Proximity coupling of superconducting nanograins with fractal distributions

Uchino, Takashi ; Teramachi, Nanami ; Matsuzaki, Ryosuke ; Tsushima, Emi ; Fujii, Shusuke ; Seto, Yusuke ; Takahashi, Kazuyuki ; Mori, Taka…

Proximity coupling of superconducting nanograins with fractal distributions

Takashi Uchino [1,*], Nanami Teramachi,[1] Ryosuke Matsuzaki,[1] Emi Tsushima,[1] Shusuke Fujii,[1] Yusuke Seto,[2]
Kazuyuki Takahashi [1], Takao Mori [3], Yutaka Adachi,[4] Yukihito Nagashima,[5] Yoshifumi Sakaguchi,[6] Kazuki Ohishi,[6]
Akihiro Koda,[7] Takahiro Sakurai,[8] and Hitoshi Ohta [9]

[1]*Department of Chemistry, Graduate School of Science, Kobe University, Nada, Kobe 657–8501, Japan*
[2]*Department of Planetology, Graduate School of Science, Kobe University, Nada, Kobe 657–8501, Japan*
[3]*International Center for Materials Nanoarchitectonics, National Institute for Materials Science, Namiki 1-1, Tsukuba 305–0044, Japan*
[4]*Optoelectonic Materials Group, Optical and Electronic Materials Unit, National Institute for Materials Science, Namiki 1-1,
Tsukuba 305–0044, Japan*
[5]*Nippon Sheet Glass Co., LTD., Konoike, Itami 664–8520, Japan*
[6]*Neutron Science and Technology Center, Comprehensive Research Organization for Science and Society (CROSS), Tokai 319–1106, Japan*
[7]*Institute of Materials Structure Science, High Energy Accelerator Research Organization, Tsukuba, Ibaraki 305–0801, Japan*
[8]*Center for Support to Research and Education Activities, Kobe University, Nada, Kobe 657–8501, Japan*
[9]*Molecular Photoscience Research Center, Kobe University, Nada, Kobe 657–8501, Japan*

We explore the electrical and magnetic properties of a fractal assembly of Josephson junctions with transparent interfaces. For this purpose, we employ an $Mg/MgO/MgB_2$ nanocomposite with ~ 16 vol. % of MgB_2 nanograins, which are distributed in a fractal manner in the normal matrix. Irrespective of the low volume fraction of MgB_2 nanograins, the nanocomposite behaves as a bulk-like superconductor, i.e., zero resistivity, perfect diamagnetism, and strong vortex pinning. Thus, a global Josephson phase coherence is achieved in the nanocomposite. The lower (H_{c1J}) and higher (H_{c2J}) critical fields of the Josephson network are exceptionally high ($H_{c1J} = 96$ Oe and $H_{c2J} = 83.5$ kOe) as compared to those reported previously for granular superconductors. This will give an example of robust macroscopic superconducting coherence derived from long-range proximity coupling among fractally distributed superconducting nanograins through quantum interference of Andreev quasiparticles. Transverse-field muon spin rotation measurements reveal that the mean internal field in the superconducting mixed state increases with decreasing temperature below which the Josephson phase coherence sets in, opposite to the diamagnetic response observed in magnetization measurements. This unusual behavior implies a highly disordered and fluctuating nature of the Josephson vortices in the present superconducting nanocomposite.

I. INTRODUCTION

In nature, we find a large set of systems consisting of many interacting components whose collective behavior cannot be predicted in terms of the components. Examples of these systems range from brain-network function to solar flare statistics [1,2]. It is also interesting to note that these complex systems often consist of hierarchical lattices with power-law distributions [3], leading to a fractal network system [3–5]. Thus, structure, dynamics, and characterization of scale-invariant fractal networks and related power-law phenomena have received considerable attention in various fields of science over the past decades [3–6]. Recently, such a scale-invariant structural organization and related structural inhomogeneity have been found to exist also in high-transition-temperature (T_c) superconductors [7–10]. It has been demonstrated [7] that even in optimally doped superconducting samples, oxygen interstitials exhibit highly inhomogeneous distributions, yielding fractal-like defect networks. This strongly suggests

the underlying relationship between scale-free structural patterns and superconducting transition temperature T_c [7–12]. In addition, it has been recognized that the fractal nature of critical wave function correlations in disordered superconductors plays a vital role in generating and enhancing superconductivity [11–18].

Motivated by these recent works, we here investigate the electrical and magnetic properties of an $Mg/MgO/MgB_2$ nanocomposite, in which the superconducting (MgB_2) nanocrystals are distributed in the normal matrix in a fractal manner. The volume fraction of superconducting MgB_2 nanocrystals in the nanocomposite is $\sim 16\%$, which is below the critical volume fraction ($\sim 20-\sim 50\%$) for the onset of percolative superconductivity in granular systems [19–21]. In spite of such a low volume fraction of the MgB_2 nanograins, the nanocomposite shows a bulk-like superconducting behavior, i.e., zero resistivity, perfect diamagnetism, and strong vortex pinning. These results indicate that a robust and global Josephson coherence is achieved in the nanocomposite, showing the occurrence of long-range proximity coupling among fractally distributed superconducting nanograins through phase coherent Andreev reflections [22,23]. We also

*uchino@kobe-u.ac.jp

investigate and discuss the internal magnetic field distribution in the nanocomposite using transverse-field muon spin rotation spectroscopy.

II. EXPERIMENTAL PROCEDURES

To fabricate a solid sintered body of the Mg/MgO/MgB$_2$ nanocomposite, we first carried out the solid phase reaction between Mg and B$_2$O$_3$ [24] in flowing Ar atmosphere (for details, see the Supplemental Material [25]). To ensure the inclusion of Mg in the products, the excess amount of Mg (Mg : B$_2$O$_3$ = 5 : 1) was employed. The expected reaction is given by

$$5\text{Mg} + \text{B}_2\text{O}_3 \rightarrow 3\text{MgO} + \text{MgB}_2 + \text{Mg}. \quad (1)$$
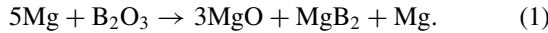
The method had been originally developed by the present authors to synthesize highly defective MgO microcrystals with a large number of oxygen vacancies [26–28]. The resulting black powders were then processed using a spark plasma sintering (SPS) system. In SPS, sintering is realized by subjecting the green compact to arc discharge generated by a pulsed electric current. An electric discharge process takes place on a microscopic level and accelerates the sintering processes accompanied by material diffusion. One of the most pronounced features of this technique is that the small grain size can be maintained while achieving full densification, enhancing the connectivity between grains through the minimization of the undesirable grain growth and the creation of clean grain boundaries [29]. Hence, the SPS treatment is a key process for preparing a densified Mg/MgO/MgB$_2$ with clean interfaces and high connectivity.

The structural, morphological, thermal, electrical, and magnetic properties of the thus obtained Mg/MgO/MgB$_2$ nanocomposite have been explored using various techniques, including x-ray diffraction (XRD), field-emission scanning electron microscopy (FESEM), high-resolution transmission electron microscopy (HR-TEM), electrical resistivity and magnetoresistivity measurements, magnetic susceptibility measurements, and transverse-field muon spin rotation (TF-μSR) spectroscopy, as described in detail in the Supplemental Material [25].

III. RESULTS

A. Structural and morphological analyses

Figure 1 shows a typical XRD pattern of the SPS-treated sample, showing the peaks assigned to Mg, MgO, and MgB$_2$. According to Scherrer equation, the average crystalline sizes d of Mg, MgO and MgB$_2$ are $d_{\text{Mg}} = 46$ nm, $d_{\text{MgO}} = 20$ nm, and $d_{\text{MgB2}} = 48$ nm, respectively. Rietveld pattern fitting [30] was then performed to determine the weight fraction of the respective crystalline phases. This resulted in a satisfactory profile fit with the weighted-profile R value (R_{wp}) of 8.11% and the goodness-of-fit (GoF) of 1.65. The weight (mole) fractions of Mg, MgO, and MgB$_2$ are estimated to be 8.5 (11.0), 78.5 (75.5), and 13.0 (13.5) %, respectively. The thus estimated mole fraction of MgO (Mg and MgB$_2$) is somewhat larger (smaller) than that expected from Eq. (1), i.e., Mg : MgO : MgB$_2$ = 20 : 60 : 20 (mole %). This is probably due to the partial oxidation of Mg during the sample preparation
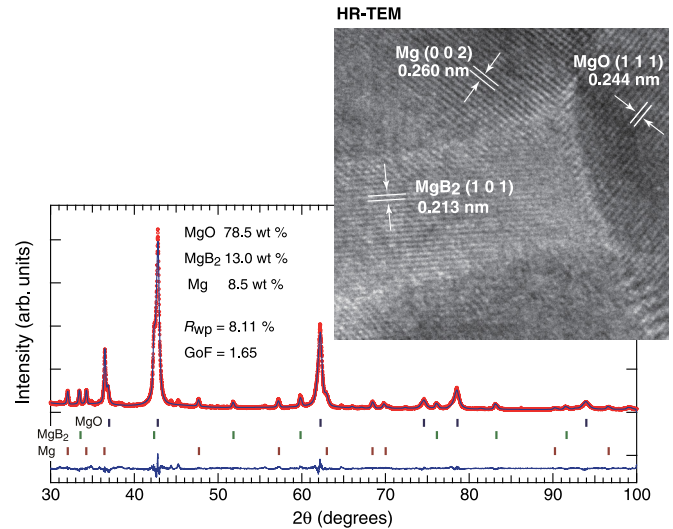

FIG. 1. Output from a Rietveld analysis of the XRD pattern. The observed data are indicated by red circles, and the calculated profile is the black continuous line overlying them. The short vertical lines below the pattern represent the positions of all possible Bragg reflections for MgO (top row), MgB$_2$ (middle row), and Mg (bottom row). The lower curve is the difference between the observed and calculated intensity at each step, plotted on the same scale. The inset shows a typical HR-TEM image obtained for Mg/MgO/MgB$_2$ interfaces.

and the post SPS processes. From the weight fractions of the constituent crystals and their bulk density, the volume fraction of the respective components are estimated to be as follows: Mg : MgO : MgB$_2$ = 15 : 69 : 16 (vol. %). This gives an upper limit of the volume fraction of the respective species, and the fraction will decrease depending on the amount of voids and/or pores possibly present in the sintered body.

Field emission scanning microscopy/energy dispersive x-ray analysis (FESEM/EDX) was performed to investigate the microstructures and chemical compositions of the nanocomposite [Figs. 2(a), 2(b)]. One sees from the lower-magnification (4k×) FESEM/EDX mapping shown in Fig. 2(a) that the elemental distributions are highly inhomogeneous. EDX quantitative elemental analysis indicates that the atomic ratio of Mg: O: B is 48: 42: 10, in reasonable agreement with that calculated based on the Rietveld quantitative analysis (Mg : O : B = 50 : 37 : 13). The FESEM/EDX mapping image also reveals that there exist red (boron) spots with a size of ~ 1 μm. This implies that the MgB$_2$ nanocrystals are aggregated to form micrometer-sized MgB$_2$-rich regions. One also sees from Fig. 2(a) that the regions of high B concentration (red spots in the boron EDX map) correspond to O-deficient regions (dark regions in the oxygen EDX map). This indicates that there exists an anticorrelation between the MgB$_2$-rich and the MgO-rich regions. It should be noted that similar inhomogeneous elemental distributions and the related anticorrelations are also seen in the higher magnified (14k×) FESEM/EDX image [Fig. 2(b)] although the size of the red spots is an order smaller than that observed in the lower magnified image. These observations demonstrate that the structural modulations induced in the nanocomposite exhibit
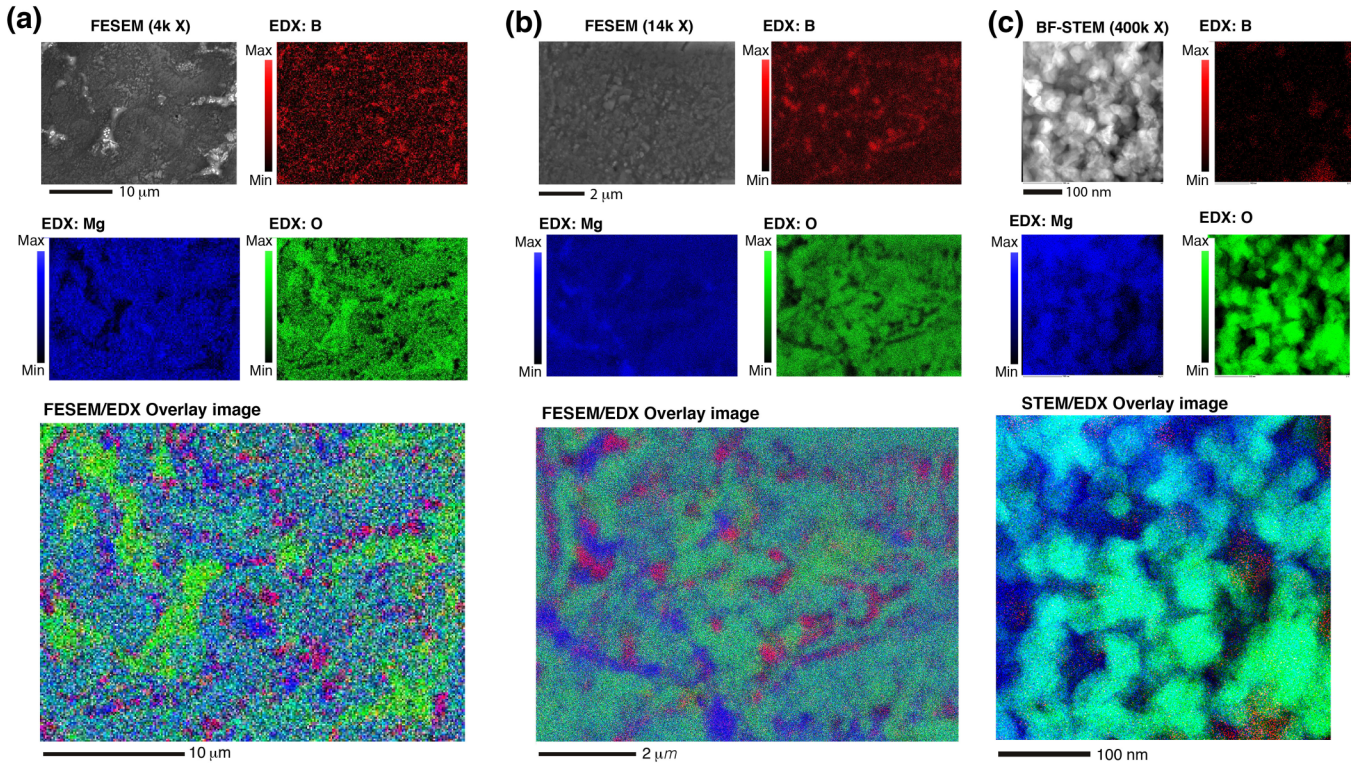
FIG. 2. FESEM and the corresponding EDX images at (a) lower (4k×) and (b) higher (14k×) magnification; Red = B, Green = O, Blue = Mg. The higher-magnified image was obtained by enlarging the O-rich region in the lower-magnified image where the micrometer-sized red spots do not appear to exist. (c) Bright field (BF)-STEM and the corresponding EDX images (400k×) for an O-rich region; Red = B, Green = O, Blue = Mg.

a self-similar (fractal-like) pattern with different hierarchical levels spanning the length scale from submicrometer to several micrometers. Such scale-invariant structural arrangements can further be identified in the scanning transition electron microscope (STEM)/EDX image shown in Fig. 2(c) (magnification 400k×), demonstrating that the primary MgO nanoparticles (green or blue-green) form chain-like clusters, and the Mg (blue) and B (red) rich regions are located in between the MgO-rich chains. From the SETM/EDX image, one sees that the respective B-rich (i.e., MgB_2-rich) regions with a size of ~50 nm are separated by a distance of more than 100 nm, which is much longer than the coherence length ξ_0 of MgB_2 ($\xi_0 = 5$ nm [31]). Thus, in the nanocomposite, the percolation channels consisting of physically connected MgB_2 nanograins will not be formed, as expected from a low volume fraction (16 vol. %) of MgB_2.

To quantitatively evaluate the fractal-like organization of the constituent elements, especially boron, we evaluated the fractal dimension by a box-counting technique [3] using various FESEM/EDX and STEM/EDX mapping images of boron with different magnifications. The box-counting technique consists of discretizing the binarized image into voxels of dimension r; the number of voxels containing the EDX signal were counted as N. Any linear dependence in the logarithmic plot of N versus r manifests fractality; the fractal dimension or box-counting dimension D was then obtained from the linear slope of the plot (for details, see the Supplemental Material [25]). We found that the box-counting curve of boron EDX mapping images shows a linear region over four orders of

magnitude of r [Fig. 3(a)]. Although the D values lie in the range from ~1.5 to ~1.7 depending on the EDX images used for the analysis [Fig. 3(b)], the fractal analysis allows us to confirm the fractal-like distribution of MgB_2 nanograins in the nanocomposite. Judging from the anticorrelation between the MgB_2-rich and the MgO-rich regions, the spatial distributions of the normal regions consisting mostly of the MgO-rich regions will not be completely random but will have scale-free characteristics as well. It should be noted, however, that when all elements (B, O and Mg) are taken into account in the box-counting procedure, the resulting D values are almost equal to 2 (see Fig. S1 in the Supplemental Material [25]), which is expected for completely random (homogeneous) distribution of points in two-dimensional images [32].

It is also worth mentioning that the interfaces among MgB_2, Mg, and MgO are atomically clean, as shown in a HR-TEM image shown in the inset in Fig. 1. In hybrid systems made of normal (N) and superconducting (S) materials with highly clean N-S interfaces, a long-range electron-hole coherence (proximity) effect is expected to persist far away from the N-S interface [33–35]. Thus, in what follows, we will investigate the electrical and magnetic properties of the composite in view of the proximity effect.

B. Electrical resistivity and magnetoresistivity measurements

Figure 4(a) presents temperature-dependent electrical resistivity $\rho(T)$ data taken at a variety of applied fields H ranging from 0 to 70 kOe. The ρ value at room
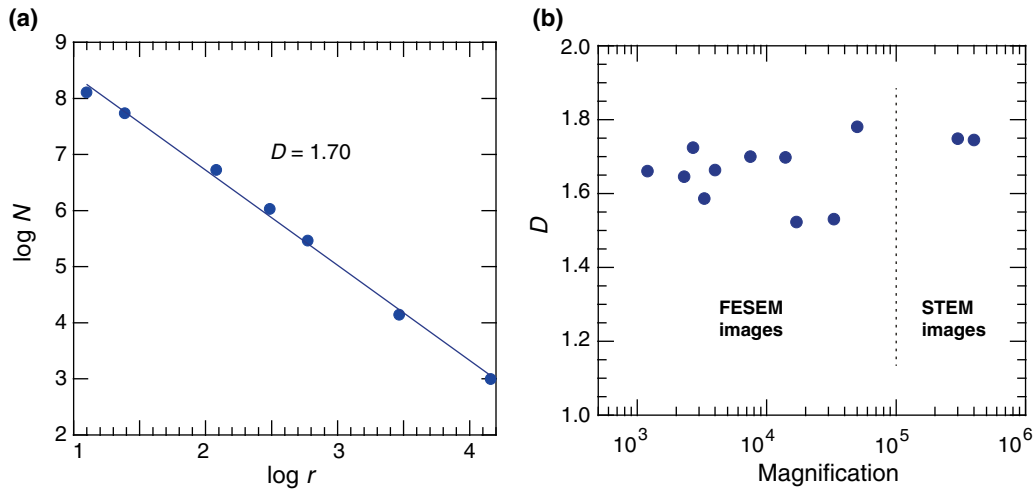
FIG. 3. (a) The box-counting analysis for boron distribution in the FESEM/EDX image given Fig. 2(a). (b) The values of D obtained for various FESEM/EDX and STEM/EDX images of boron with different magnifications.

temperature is rather low ($\rho \sim 6 \times 10^{-1}\,\mu\Omega\,\text{m}$). When taken into consideration with the fact that the composite consists of 69 vol. % of MgO, we expect that the major MgO component will not inhibit electrical conduction, but may act as good tunneling conductors due probably to oxygen vacancies [36] that are likely to be introduced during the preparation process [27]. In zero applied field, the resistivity decreases almost linearly with temperature T down to $\sim$40 K. As for the pure MgB_2 [37] and the MgB_2-MgO composite near the percolation threshold [24], $\rho(T)$ exhibits a strong power-law dependence with T, which is well approximated by $\rho(T) = \rho_0 + \rho_1 T^\alpha$ with $\alpha = 2.3 - 3$. It is hence probable that in the nanocomposite, the electrical conduction at temperatures above $\sim$40 K is not governed by the percolative conduction of MgB_2, but rather by that of Mg, which shows a linear T dependence of ρ due to lattice-scattering-limited conductivity [38]. Figure 2(a) also shows that, in zero applied field, $\rho(T)$ exhibits T_c onset at 38.5 K and becomes virtually zero ($\rho <\sim 10^{-11}\,\Omega\text{m}$) at temperatures below 33.4 K, implying the establishment of the intergrain Josephson network of MgB_2 nanograins. Thus, the zero-field resistivity below T_c(onset) does not show a broad tail, although a broad exponential tail is often observed in disorder superconductors near the percolation threshold [39,40]. Residual resistivity ratio [RRR $= \rho(300\,\text{K})/\rho(39\,\text{K})$] is rather high (RRR $= 10.2$), suggesting excellent grain connectivity. Figure 4(a) further reveals that there is a large magnetoresistance $\Delta\rho/\rho_0$, where ρ_0 is the zero-field resistivity in the normal state; for example, at $H = 70\,\text{kOe}$, $\Delta\rho/\rho_0$ is $\sim$80%. This observation is somewhat surprising because a large magnetoresistance would not be observed in samples with enhanced impurity and/or defect scattering [41,42], which might be the case in general for nanocomposites. Although the origin of the large magnetoresistance is not clear at the moment, it can be said that the present nanocomposite has a long mean free path that is essential for having a large magnetoresistance. The isothermal $\Delta\rho/\rho_0$ data shown in Fig. 4(b) vary almost linearly with H, in contrast to the case of MgB_2, where $\Delta\rho/\rho_0$ shows a power-law H dependence with an exponent

of $\sim$2 [41,43]. To further investigate the magnetoresistance properties, a Kohler plot, i.e., $\Delta\rho/\rho_0$ vs H/ρ_0 on a log−log plot, is shown in Fig. 4(c). According to the Kohler′s rule, if there is a single species of charge carrier and the single scattering time, the magnetoresistance data accumulated from different temperatures should collapse to a single curve in the Kohler plot [41]. Figure 4(c) demonstrates that the Kohler′s rule is not strictly obeyed in the present sample, as expected from the composite nature of the specimen.

In the present nanocomposite, the zero resistivity state will not be realized unless the phase locking of the Josephson coupling between MgB_2 nanograins remains in effect. Hence, it would be reasonable to assume that the transition temperature at zero resistivity T_c, T_c (offset), for a given value of H can be used to evaluate the upper critical field of the Josephson network $H_{c2J}(T)$. Figure 4(d) presents the $H_{c2J}(T)$ data that we deduce from T_c(offset) in different fields shown in Fig. 4(a). The $H_{c2J}(T)$ curve shows a positive upward curvature over the entire temperature region investigated. The result is in contrast to the case of granular superconductors in the dirty limit [44], in which $H_{c2J}(T)$ shows a linear temperature dependence. We found that the $H_{c2J}(T)$ data can be well approximated by the expression $H_{c2J}(T) = H_{c2J}(0)(1 - T/T_c)^{1+\alpha}$. The fitted values of $H_{c2J}(0)$ and α are 83.5 kOe and 0.28, respectively. Typical H_{c2} values of granular high-T_c superconductors are less than $\sim$30 Oe [45]. Thus, the estimated value of $H_{c2J}(0)$ is unusually high, implying that the enhanced phase-locked state is realized in the present nanocomposite.

C. Magnetization measurements

Figure 5 shows the results of magnetization M measurements of the nanocomposite. From the magnified view of magnetic susceptibility ($4\pi\chi$ or $4\pi M/H$) measured in $H = 5\,\text{Oe}$ [see the inset of Fig. 5 (a)], one sees that the transition from the normal to the superconducting state begins at $\sim$38 K, in agreement with the zero field resistivity measurement. Figure 5(a) also demonstrates that the $4\pi\chi$ value observed in the zero field cooled (ZFC) state reaches almost -1 for $T <\sim 10$
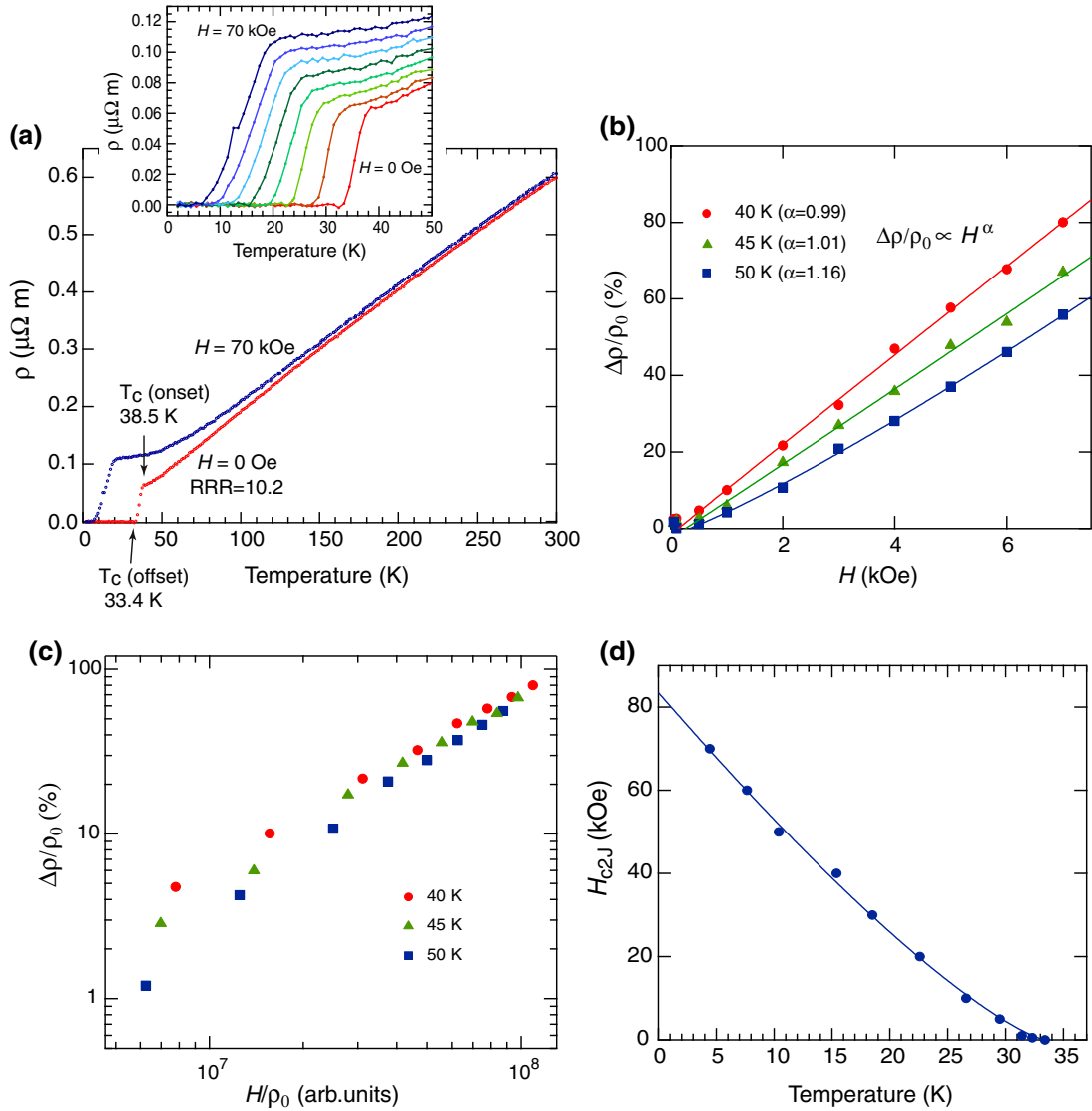
FIG. 4. (a) Resistivity of the Mg/MgO/MgB$_2$ nanocomposite in zero and in 70 kOe applied field. The inset shows a magnified view of resistive superconducting transition in different applied fields (from bottom right to top left) from 0 to 70 kOe in steps of 10 kOe. (b) Magnetic field dependence of the isothermal magnetoresistance $\Delta\rho/\rho_0$. The solid lines are fitting curves of $\Delta\rho/\rho_0 \propto H^\alpha$ to the experimental data. (c) Kohler plot obtained from the data shown in (b). (d) Upper critical field of the Josephson coupled network H_{c2J} determined from T_c(offset) in different H. The solid line represents the fit of the function $H_{c2J}(T) = H_{c2J}(0)\,(1 - T/T_c)^{1+\alpha}$. The fitted values of $H_{c2J}(0)$ and α are 83.5 kOe and 0.28, respectively.

K and $H < {\sim}20$ Oe. This reveals that a state of the perfect diamagnetism, i.e., bulk-like superconductivity, is achieved in the composite. On the other hand, the field cooled (FC) curves show a very low Meissner fraction ($< {\sim}1\%$), demonstrating strong pinning in the sample (see also the $M(H)$ hysteresis loops shown in Fig. S2 in the Supplemental Material [25]).

The temperature dependence of the initial $M(H)$ curves is shown in Fig. 5(b). The initial slope becomes steeper with decreasing temperature from 36 to ${\sim}30$ K [see also the right axis of Fig. 5(d) and Fig. S3 [25]]. This probably arises from a decrease in the intragrain penetration depth with decreasing temperature. Figure 5(b) further demonstrates that at temperatures below ${\sim}28$ K, an additional diamagnetic component with a much steeper slope begins to emerge in the low H ($H < {\sim}10$ Oe) region, due to the establishment of intergrain Josephson coupling. We also found that in the temperature

range below ${\sim}30$ K down to ${\sim}20$ K, the initial $M(H)$ curves exhibit periodic magnetization jumps, as shown in the inset of Fig. 5(b) (see also Fig. S3 [25]). Such oscillating $M(H)$ signals have been reported in mesoscopic superconductors [46,47] and are understood qualitatively as an entry or exit of magnetic vortices, arising from size quantization of the Cooper-pair motion [46]. Thus, in the temperature range between ${\sim}20$ and ${\sim}30$ K, the system can be regarded as a simple (noninteracting) assembly of mesoscopic Josephson junction loops. With a further decrease in temperature below ${\sim}20$ K, the initial magnetization does not show such an oscillating behavior but begins to exhibit a simple linear decrease with H with a slope $-dM/dH$ of ${\sim}1/4\pi$ up to a certain H value [see Fig. 5(c) and Fig. S3 [25]]. This implies that the respective mesoscopic Josephson loops interact coherently to generate a macroscopic Josephson system, leading to a bulk-like superconducting
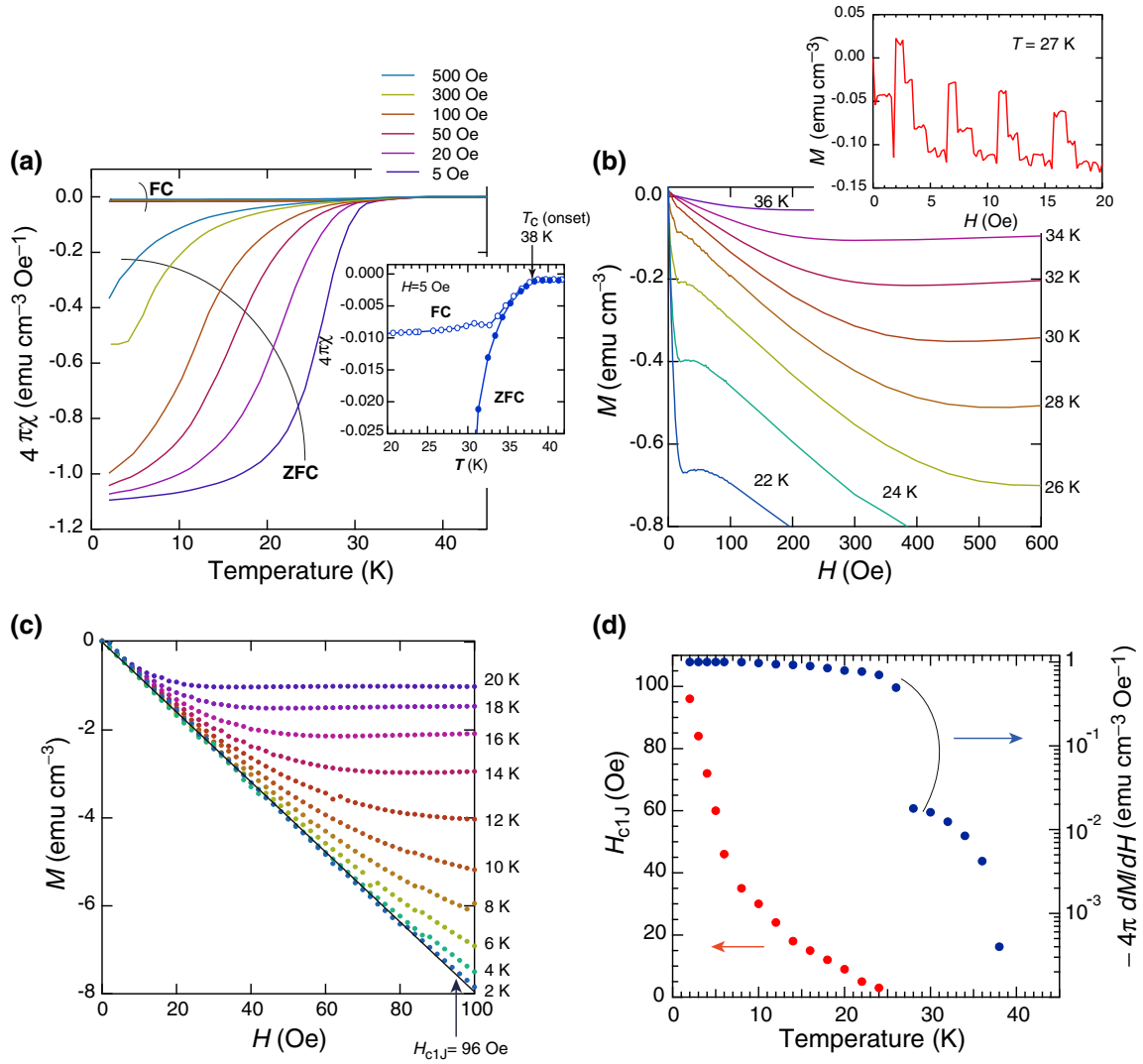
FIG. 5. (a) Zero-field-cooling (ZFC) and field-cooling (FC) magnetic susceptibility curves measured under different applied fields H. The inset shows a magnified view of the susceptibility curves at $H = 5$ Oe around the transition region. (b) Zero-field-cooled magnetization $M(H)$ initial curves in temperature range from 22 to 36 K. The inset shows a magnification of the initial $M(H)$ curve at 27 K in the 0–20 Oe region. (c) Zero-field-cooled $M(H)$ curves in the temperature range from 2 to 20 K. The black line indicates the line with a slope of $-1/4\pi$ showing the case of perfect diamagnetism. (d) Josephson lower critical field H_{c1J} (left axis) and $-4\pi(dM/dH)$ (right axis) as a function of temperature.

response. The point of departure from linearity will represent the lower critical field of the Josephson-coupled (intergrain) superconducting network H_{c1J}. The temperature dependence of $H_{c1J}(T)$ is shown in the left axis of Fig. 5(d). One sees a steep increase in $H_{c1J}(T)$ with decreasing temperature below ~ 10 K, reaching the value of 96 Oe at 2 K. The resulting H_{c1J} value is about two orders of magnitude larger than that observed commonly in granular high-T_c superconductors [45].

In type-II superconductors, the upper critical field H_{c2} represents the field value for which the distance between two fluxons approaches the order of coherence length ξ. According to the GL theory, the relationship between H_{c2} and ξ is given by [48]

$$H_{c2} = \Phi_0/(2\pi\xi^2), \tag{2}$$

where Φ_0 is a flux quantum ($\Phi_0 = h/2e \sim 2.1 \times 10^{-15}$ Wb). If we apply this relationship to our system, we obtain a value

of $\xi_J = 6$ nm for $H_{c2J}(0) = 83.5$ kOe. The GL theory also predicts the following relationship between H_{c1} and $\kappa = \lambda/\xi$ for a high-κ superconductor ($\kappa \gg 1$) [48],

$$H_{c1} = \frac{\Phi_0}{4\pi\lambda^2}\ln\kappa. \tag{3}$$

From Eq. (3), λ_J is calculated to be 252 nm, assuming that $\xi_J = 6$ nm and $H_{c1J} = 96$ Oe. The thus obtained values of ξ_J and λ_J are consistent with the initial assumption of $\kappa = \lambda_J/\xi_J \sim 42 \gg 1$. Hence, we consider that the high-κ approximation is justified in our case and can be reasonably used to estimate the basic physical properties of the induced superconducting phase.

D. Muon spin rotation (μSR) measurements

To gain further insight into the superconducting state of the nanocomposite, we carried out μSR measurements [49]
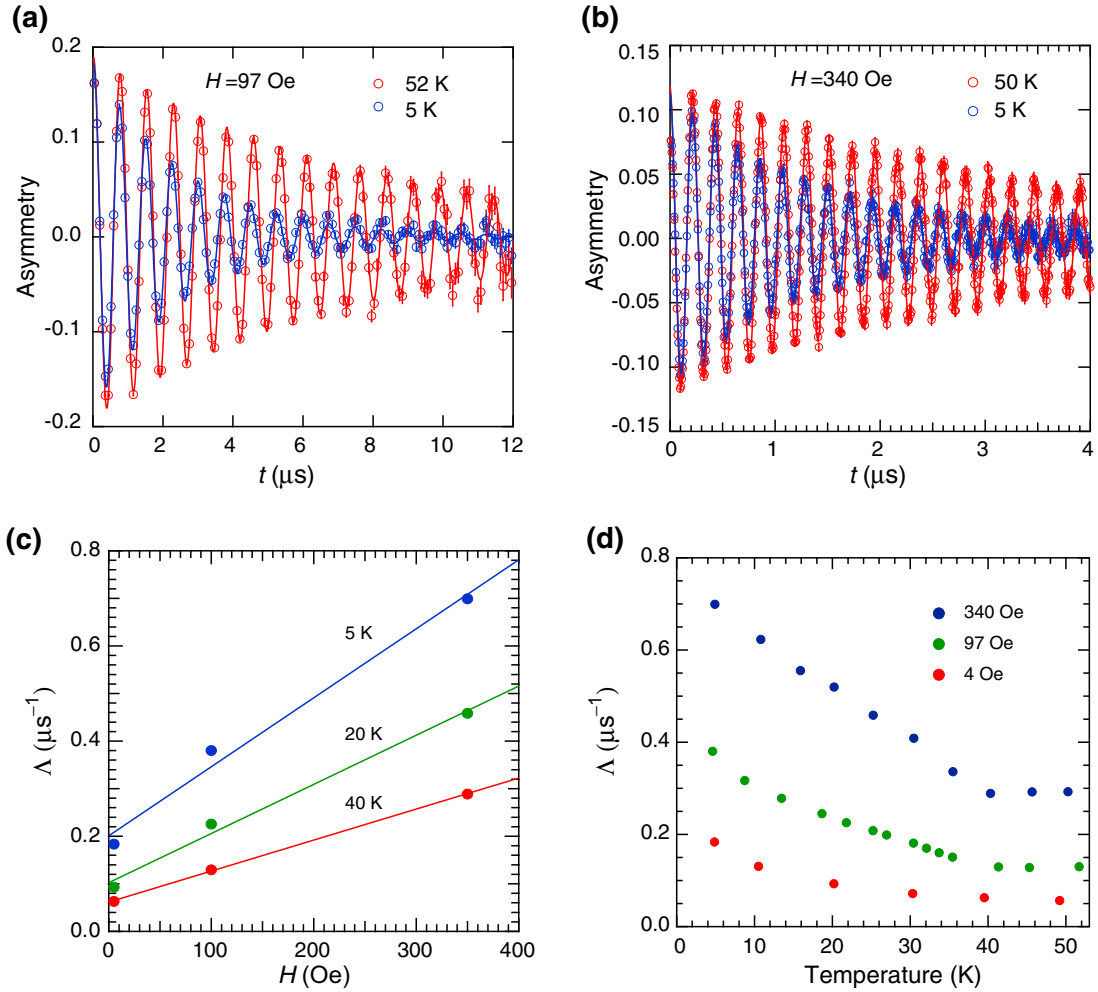
FIG. 6. Transverse-field (TF) μSR time spectra collected above and below T_c under field cooled conditions at (a) $H = 97$ Oe and (b) 340 Oe. The solid lines are the fit to the data using a Lorentzian field distribution described in Eq. (5). (c) Field dependence of the Lorentzian relaxation rate Λ obtained under different temperatures. The solid lines are the linear fit to the data. (d) Temperature dependence of Λ obtained under different applied fields. In (c) and (d), errors are within the size of the symbols.

in applied transverse fields (TFs). TF-μSR has proved an effective probe of the internal magnetic field distributions $n(B)$ in the vortex state of conventional and unconventional type-II superconductors [50,51]. In this work, high-statistics of $\sim 100 \times 10^6$ muon decay events were collected in magnetic fields applied transverse to the initial muon spin polarization $P(t = 0)$. The TF-μSR signal is the time t evolution of $P(t)$, and is related to $n(B)$ by the following relationship [50,51]:

$$P(t) = \int_0^\infty n(B) \exp(i\gamma_\mu B t) dB, \tag{4}$$

where γ_μ is the muon gyromagnetic ratio. When the TF-μSR signal is measured in the time domain, its Fourier transform provides a good approximation of $n(B)$.

Figures 6(a) and 6(b) shows the TF-μSR spectra of the sample in the normal and superconducting states measured in FC conditions in fields of 97 and 340 Oe. We found that the profiles of $P(t)$ obtained at temperatures above T_c are well fitted by the oscillatory decaying Lorentzian function,

$$AP(t) = A \exp(-\Lambda t) \cos(\gamma_\mu \langle B \rangle t + \varphi), \tag{5}$$

where Λ is the muon relaxation rate, $\langle B \rangle$ is the central magnetic field, and φ is the initial phase angle, and A represents the initial muon asymmetry. When the magnetic-field broadening is due to nuclear dipolar fields of randomly (homogeneously) distributed ^{11}B in a sample, the time evolution is described by a Gaussian function [49]. Thus, the observed Lorentzian decay does not match the random distribution scheme, but suggests a dilute [52] and highly inhomogeneous distribution [53] of the B nuclear moment, as indeed demonstrated in the EDX mapping data shown in Fig. 2. The dilute distribution model is consistent with the observation that in the normal state, Λ grows linearly with applied field up to 340 Oe [see the red filled circles in Fig. 4(c)]. At temperatures well below T_c, e.g., $T = 5$ K, the TF-μSR signals, which can be still fitted reasonably with the same Lorentzian function as described in Eq. (5), decay almost completely with negligible background signal, meaning that the Josephson-coupled superconductivity extends throughout the sample volume. Note also that, as shown in Fig. 4(c), Λ shows a linear increase with H both at temperatures of 5 and 20 K, as in the case of the normal state. These results allow us to expect that under this experimental condition,
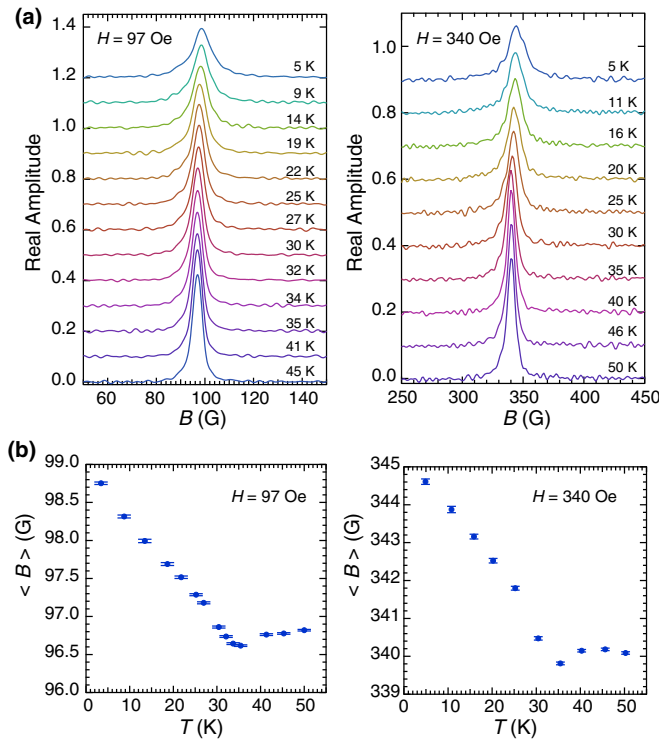
FIG. 7. (a) Temperature-dependent variations of the real amplitude of the FFT of the TF-μSR time spectra obtained under magnetic fields of 97 (left panel) and 340 Oe (right panel). (b) Temperature dependence of the fitted central magnetic field $\langle B \rangle$ obtained under applied fields of 97 (left panel) and 340 Oe (right panel). The fitting errors are shown as horizontal bars.

the internal field distribution becomes more inhomogeneous with increasing H, and the vortices are well separated to each other on the length scale of the Josephson penetration depth. It is hence interesting to investigate the fast Fourier transformation (FFT) of the TF-μSR spectra [see Fig. 7(a)], providing an approximate picture of the $n(B)$ probed by the muons. One sees from Fig. 7(a) that rather symmetric line shapes are observed both at temperatures below and above T_c. In general, the magnetic disorder induced by random pinning in the superconducting mixed state will truncate the high-field tail and reduce the asymmetry of the line shape [54,55]. Thus, the symmetric nature of the $n(B)$ spectra is attributed to the random pinning centers present in the nanocomposite. One also notices that the peak field tends to become higher than the applied field with decreasing T and/or increasing H. To further quantify the temperature dependence of the peak field, we plot in Fig. 7(b) the fitted values of $\langle B \rangle$, which represents the maximum in the $n(B)$ spectra, as a function of temperature. One sees a slight negative shift right below T_c, both for $H = 97$ and 340 Oe, whereas at temperatures below $\sim$30 K the $\langle B \rangle$ value shows a positive shift with decreasing temperature. This is in contrast to the case of typical type-II superconductors, in which the peak maxima, which represent the smeared-out van Hove singularities, are displaced below the external magnetic field due to flux expulsion [49–51]. A possible origin of this unusual behavior will be discussed in Sec. IV.

Figure 6(d) reveals that the muon relaxation rate Λ shows an almost linear T dependence even in the temperature region well below T_c. This is in contrast to a T independent behavior observed in the two-gap (s-wave) superconductor MgB_2 [56,57]. A similar linear T dependence of the relaxation rate has been observed in the high-T_c cuprate [58] and Fe-based [59] superconductors and is often interpreted in terms of the presence of nodes in the energy gap function [51,59]. However, the nodal gap scenario cannot be applied to the present $Mg/MgO/MgB_2$ nanocomposite system. The observed linear T dependence results from a different mechanism, presumably phase fluctuation of the superconducting order parameter [60,61], as will be discussed also in Sec. IV.

IV. DISCUSSION

The TF-μSR experiments have demonstrated that the internal magnetic field distributions in the present nanocomposite are quite different from those in typical type-II superconductors, as evidenced, for example, by a paramagnetic signature under applied fields. Figure 7(b) shows that the paramagnetic shift is observed especially at temperatures below $\sim$30 K. This indicates that the vortices penetrating the Josephson coupled regions, i.e., the Josephson vortices, are responsible for the observed paramagnetic shift. Previous μSR measurements have demonstrated that only a few classes of high-temperature superconductors (HTS), including electron-doped cuprate superconductors ($Pr_{2-x}Ce_xCuO_4$ [62] and $Pr_{1-x}LaCe_xCuO_4$ [63]) and Fe-based superconductors ($Sr(Fe_{1-x}Co_x)_2As_2$ [64,65] and $Ba(Fe_{1-x}Co_x)_2As_2$ [55,65]), show a similar paramagnetic shift. Although the physical origin has not been fully understood, the field-induced magnetic order derived, directly or indirectly, from the d and/or f metals in these HTS materials are assumed to be responsible for the observed paramagnetic signature [62,64,65]. We should note that the present superconducting nanocomposite does not nominally contain any such d and/or f block elements, implying that its origin is different from that in the HTS. We can also rule out the possibility of explaining the positive field shift by the so-called paramagnetic Meissner effect [66,67] because both ZFC and FC magnetization data show a diamagnetic shift [see Fig. 5(a)].

Irrespective of its origin, the observed paramagnetic shift indicates that the Josephson vortices in our sample have core regions, since in the superconducting mixed state, only the field in the vortex core carrying a flux quantum can exceed the external field [68]. This is consistent with the recent prediction [69] and observation [70] that Josephson vortices in long diffusive SNS Josephson junctions have real cores. As for an ideal vortex lattice, the core regions contribute to the high-field tail of the local magnetic field distribution [50,51]. In the present superconducting nanocomposite, however, the high-fields tail is truncated to yield a rather symmetric distribution [see Fig. 7(a)]. This implies substantial disordering of the vortices. We suggest that the vortex disordering occurs not only in a static but also in a dynamic way; that is, dynamic variation of the vortex positions is likely to take place due to phase fluctuations of the superconducting order parameter in the Josephson network on a time scale faster than the characteristic muon sampling time ($\sim$10 μs). Considering that
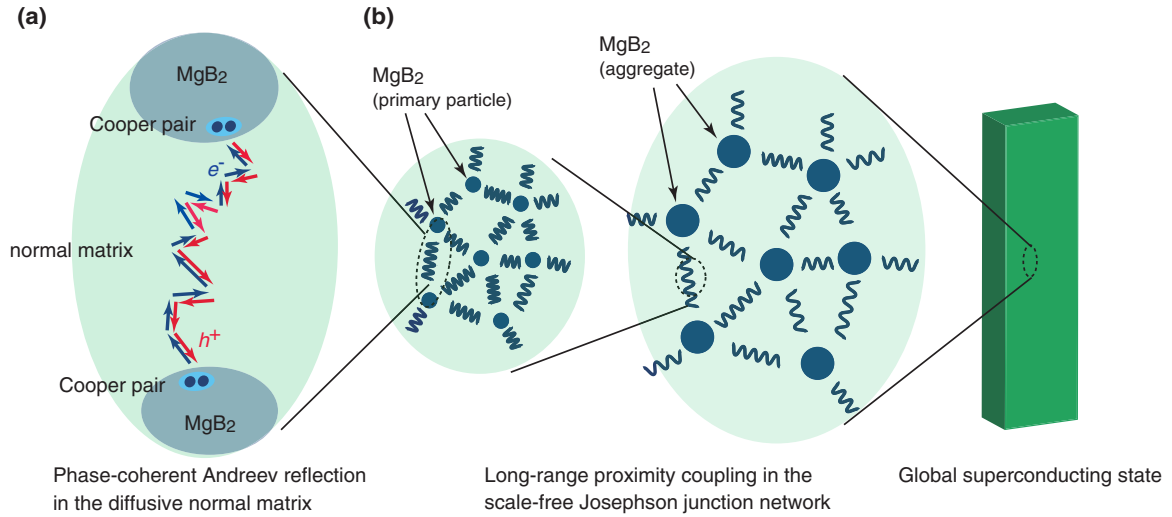
FIG. 8. Schematic illustration of the superconducting proximity effect in the Mg/MgO/MgB$_2$ nanocomposite. (a) The Andreev refroreflection at the MgB$_2$/Mg(MgO)/MgB$_2$ interfaces where diffusive counterpropagation of electron- and hole-like quasiparticles with zero total phase accumulation is possible. (b) Development of the long-range proximity coupling in the fractal Josephson network consisting of MgB$_2$ nanograins with hierarchical length scales (left and middle panels), leading to a global superconducting state (right panel).

the static disordering will not be sufficient to account for the observed paramagnetic shift [71], we could suggest that such phase fluctuations are responsible for the unusual paramagnetic behaviors probed by TF-μSR. In granular systems, quantum phase fluctuations are inevitable because the charge, which is quantum conjugate to the phase, on each grain is assumed to be constant [72]. As noted earlier, the expected phase fluctuations are also supported by an almost linear T dependence of the muon relaxation rate [see Fig. 4(c)]. It is also likely that the scale-invariant Josephson network induces dynamic or nonequilibrium vortex states characterized by intense fluctuation behavior, which has been shown to play an important role in a vortex insulator-to-metal transition in a proximity array of superconducting islands [73,74]. The fluctuating nature of the Josephson vortices could be inherent to the fractal disorder, leading to the underlying nonequilibrium critical phenomena.

It should be noted, however, phase fluctuations generally compete with Josephson coupling. It is probable that in the present Josephson coupled system, there exists a mechanism that facilitates a global phase locking irrespective of the presence of substantial phase fluctuations. The criterion for the granular superconductors to become phase locked is [75]

$$zE_J \geqslant k_BT + E_C, \qquad (6)$$

where E_J is the Josephson coupling energy, E_C is the charging energy, and z is a parameter of the order of the number of the neighboring grains contributing to the phase locking. In usual granular superconductors, z should be taken as the number of the nearest neighbors around each superconducting grain [71,75]. However, the number of z could be much larger if respective superconducting grains interact fractally and hierarchically to form a macroscopic scale-free network, and accordingly the condition to achieve a global phase locking will become easier to fulfill. Recently, scale-invariant antiferromagnetic textures with robust and nonvolatile characteristics have been shown to exist in NdNiO$_3$ [76], which is one of the

strongly correlated quantum solids. It has been demonstrated that in NdNiO$_3$, the close interplay between competing phases triggers new organizing principles, resulting in the robust electronic fabric textures with a scale-free power-law distribution [76]. Thus, scale-invariant magnetic textures will generally have a potential to induce emergent but stable electronic and magnetic phases on the verge of criticality.

From the microscopic point of view, the superconducting proximity effect is the result of an interplay between Andreev reflection and phase coherence in NS junctions [77,78]. In the Andreev reflection process, an electron (e^-) in the N conductor is retroreflected as a hole (h^+) along the time-reversed path of the electron (and vice versa), and the missing charge of $2e^-$ is absorbed as a Cooper pair by the S region. The degree of proximity coupling and phase shift can be influenced by a number of factors, including the energy of the incident electron, the path length of the electron and the retroreflected hole, the applied magnetic field, the transparency of NS interfaces, and the disorder in the N region [77–79]. In particular, the presence of disorder (or elastic scatters) is important because the multiple elastic scattering process in the N region leads to diffusive counterpropagation with zero total phase accumulation, resulting in the so-called reflectionless tunneling [79]. Note also that the reflectionless tunneling requires highly transparent NS interfaces [33–35]. Considering that the present nanocomposite is characterized by atomically clean interfaces (see the inset of Fig. 1), we suggest that the coherent multiple scattering process occurs in between the adjacent, but remote, MgB$_2$ nanograins, as illustrated in Fig. 8(a). It would be possible that the collective accumulation of respective coherent transfer processes through the N-S interface result in coherent closed loops where the total phase shift eventually becomes zero. When the superconducting grains are distributed in a fractal manner, it would also be expected that phase coherent loops with different sizes are hierarchically interacted with each other through Andreev bound states [80] to develop into macroscopic Josephson junctions [see

Fig. 8(b)]. Such a self-organized network often arises in scale-free fractal systems [1–4] and is believed to be created through a feedback between different dynamical and the underlying correlation and percolation properties of the network [81]. This leads to global coherence or synchronization [82] and induces the emergent electronic and magnetic phases near a critical point [76], as mentioned earlier. We suggest that this hierarchical feedback mechanism is responsible for the increase in z in Eq. (6) and hence the occurrence of the bulklike superconductivity in the present nanocomposite system.

V. CONCLUSIONS

We have investigated the superconducting properties of the nanocomposite with clean atomic interfaces, in which the MgB_2 nanograins are distributed in a fractal manner. Although the volume fraction of MgB_2 grains ($\sim$16 vol. %) appears to be too low to form percolation channels of their own, the global Josephson phase coherence is induced in the nanocomposite. The lower (H_{c1J}) and higher (H_{c2J}) critical fields of the Josephson network are exceptionally high ($H_{c1J} = 96$ Oe, and $H_{c2J} = 83.5$ kOe). From the values of H_{c1J} and H_{c2J}, ξ_J and λ_J are estimated to be 6 and 252 nm, respectively. Thus, the resulting Josephson coupled state can be practically regarded as a bulk type-II superconductor. However, the magnetic field distributions probed by the TF-μSR measurements are quite different from those in typical type-II superconductors. The vortex lattices will not be simply aligned parallel to the applied field, but will exhibit strong misalignment with dynamic fluctuations, leading to the paramagnetic response. We suggest that the collective effect due to Andreev reflection in the scale-free Josephson network is responsible for the establishment of the robust proximity coupling and the unusual internal magnetic field distribution.

[1] H. J. Jensen, *Self-Organized Criticality: Emergent Complex Behavior in Physical and Biological Systems* (Cambridge University Press, Cambridge, 1998).

[2] C. J. Stam, Modern network science of neurological disorders, Nat. Rev. Neurosci. **15**, 683 (2014).

[3] M. Schroeder, *Fractals, Chaos, Power Laws: Minutes from an Infinite Paradise* (Freeman, New York, 1991).

[4] B. B. Mandelbrot, *The Fractal Geometry of Nature (London)* (Freeman, San Francisco 1982).

[5] C. Song, S. Havlin, and H. A. Makse, Origins of fractality in the growth of complex networks, Nat. Phys. **2**, 275 (2006).

[6] S. N. Kempkes, M. R. Slot, S. E. Freeney, S. J. M. Zevenhuizen, D. Vanmaekelbergh, I. Swart, and C. M. Smith, Design and characterization of electrons in a fractal geometry, Nat. Phys. **15**, 127 (2019).

[7] M. Fratini, N. Poccia, A. Ricci, G. Campi, M. Burghammer, G. Aeppli, and A. Bianconi, Scale-free structural organization of oxygen interstitials in La$_2$CuO$_{4+y}$, Nature (London) **466**, 841 (2010).

[8] B. Phillabaum, E. W. Carlson, and K. A. Dahmen, Spatial complexity due to bulk electronic nematicity in a superconducting underdoped cuprate, Nat. Commun. **3**, 915 (2012).

[9] N. Poccia, A. Ricci, G. Campi, M. Fratini, A. Puri, D. Di Gioacchino, A. Marcelli, M. Reynolds, M. Burghammer, N. L. Saini, G. Aeppli, and A. Bianconi, Optimum inhomogeneity of local lattice distortions in La$_2$CuO$_{4+y}$, PNAS **109**, 15685 (2012).

[10] G. Campi, A. Bianconi, N. Poccia, G. Bianconi, L. Barba, G. Arrighetti, D. Innocenti, J. Karpinski, N. D. Zhigadlo, S. M. Kazakov, M. Burghammer, M. v. Zimmermann, M. Sprung, and A. Ricci, Inhomogeneity of charge-density-wave order and quenched disorder in a high-T_c superconductor, Nature (London) **525**, 359 (2015).

[11] J. Zaanen, The benefit of fractal dirt, Nature (London) **466**, 825 (2010).

[12] E. W. Carlson, Charge topology in superconductors, Nature (London) **525**, 329 (2015).

[13] M. V. Feigel'mana, L. B. Ioffe, V. E. Kravtsov, and E. Cuevas, Fractal superconductivity near localization threshold, Ann. Phys. **325**, 1390 (2010).

[14] M. N. Gastiasoro and B. M. Andersen, Enhancing superconductivity by disorder, Phys. Rev. B **98**, 184510 (2018).

[15] T. Dubouchet, B. Sacépé, J. Seidemann, D. Shahar, M. Sanquer, and C. Chapelier, Collective energy gap of preformed Cooper pairs in disordered superconductors, Nat. Phys. **15**, 233 (2019).

[16] G. Bianconi, Enhancement of T_c in the superconductor–insulator phase transition on scale-free networks, J. Stat. Mech. (**2012**) P07021.

[17] N. Poccia, A. Ricci, and A. Bianconi, Fractal structure favoring superconductivity at high temperatures in a stack of membranes near a strain quantum critical point, J. Supercond. Novel Mag. **24**, 1195 (2011).

[18] N. Poccia, M. Lankhorst, and A. A. Golubov, Manifestation of percolation in high temperature superconductivity, Physica C: Supercond. Appl. **503**, 82 (2014).

[19] G. Eytan, R. Rosenbaum, D. S. McLachlan, and A. Albers, Resistivity and magnetoresistivity measurements near the metal-insulator and superconductor-insulator transition in granular Al-Ge, Phys. Rev. B **48**, 6342 (1993).

[20] A. Gerber, A. Milner, G. Deutscher, M. Karpovsky, and A. Gladkikh, Insulator-Superconductor Transition in 3D Granular Al-Ge Films, Phys. Rev. Lett. **78**, 4277 (1997).

[21] X. Liu, R. P. Panguluri, Z.-F. Huang, and B. Nadgorny, Double Percolation Transition in Superconductor-Ferromagnet Nanocomposites, Phys. Rev. Lett. **104**, 035701 (2010).

[22] A. F. Andreev, The thermal conductivity of the intermediate state in superconductors, Zh. Eksp. Teor. Fiz. **46**, 1823 (1964) [Sov. Phys. JETP. **19**, 1228 (1964)].

[23] P. Dubos, H. Courtois, O. Buisson, and B. Pannetier, Coherent Low-Energy Charge Transport in a Diffusive S-N-S Junction, Phys. Rev. Lett. **87**, 206801 (2001).

[24] Y. B. Zhang, D. F. Zhou, Z. X. Lv, Z. Y. Deng, C. B. Cai, and S. P. Zhou, Electrical transport characteristics of superconducting MgB_2–MgO composite near continuous percolation, J. Appl. Phys. **107**, 123907 (2010).

[25] See Supplemental Material at http://link.aps.org/supplemental/10.1103/PhysRevB.101.035146 for the experimental and analysis details and additional $M(H)$ data.

[26] T. Uchino and D. Okutsu, Broadband Laser Emission from Color Centers Inside MgO Microcrystals, Phys. Rev. Lett. **101**, 117401 (2008).

[27] Y. Uenaka and T. Uchino, Photoexcitation, trapping, and recombination processes of the F-type centers in lasing MgO microcrystals, Phys. Rev. B **83**, 195108 (2011).

[28] T. Uchino, Y. Uenaka, H. Soma, T. Sakurai, and H. Ohta, Magnetic hysteresis behavior and magnetic pinning in a d° ferromagnet/superconductor nanostructure, J. Appl. Phys. **115**, 063910 (2014).

[29] P. Cavaliere (Ed.), *Spark Plasma Sintering of Materials* (Springer, Cham, 2019).

[30] L. B. McCusker, R. B. Von Dreele, D. E. Cox, D. Louër, and P. Scardi, Rietveld refinement guidelines, J. Appl. Cryst. **32**, 36 (1999).

[31] P. C. Canfield, S. L. Bud'ko, and D. K. Finnemore, An overview of the basic physical properties of MgB_2, Physica C: Supercond. **385**, 1 (2003).

[32] S. R. Forrest and T. A. Witten Jr., Long-range correlations in smoke-particle aggregates, J. Phys. A **12**, L109 (1979).

[33] A. Yu. Kasumov, O. V. Kononenko, V. N. Matveev, T. B. Borsenko, V. A. Tulin, E. E. Vdovin, and I. I. Khodos, Anomalous Proximity Effect in the Nb-BiSb-Nb Junctions, Phys. Rev. Lett. **77**, 3029 (1996).

[34] P. Dubos, H. Courtois, B. Pannetier, F. K. Wilhelm, A. D. Zaikin, and G. Schön, Josephson critical current in a long mesoscopic S-N-S junction, Phys. Rev. B **63**, 064502 (2001).

[35] J. C. Hammer, J. C. Cuevas, F. S. Bergeret, and W. Belzig, Density of states and supercurrent in diffusive SNS junctions: Roles of nonideal interfaces and spin-flip scattering, Phys. Rev. B **76**, 064514 (2007).

[36] F. Schleicher, U. Halisdemir, D. Lacour, M. Gallart, S. Boukari, G. Schmerber, V. Davesne, P. Panissod, D. Halley, H. Majjad, Y. Henry, B. Leconte, A. Boulard, D. Spor, N. Beyer, C. Kieber, E. Sternitzky, O. Cregut, M. Ziegler, F. Montaigne, E. Beaurepaire, P. Gilliot, M. Hehn, and M. Bowen, Localized states in advanced dielectrics from the vantage of spin- and symmetry-polarized tunnelling across MgO, Nat. Commun. **5**, 4547 (2014).

[37] D. K. Finnemore, J. E. Ostenson, S. L. Bud'ko, G. Lapertot, and P. C. Canfield, Thermodynamic and Transport Properties of Superconducting Mg $^{10}B_2$, Phys. Rev. Lett. **86**, 2420 (2001).

[38] T. Ying, H. Chi, M. Zheng, Z. Li, and C. Uher, Low-temperature electrical resistivity and thermal conductivity of binary magnesium alloys, Acta Mater. **80**, 288 (2014).

[39] S.-Y. Hsu and J. M. Valles, Jr., Magnetic-field-induced pair-breaking effects in granular Pb films near the superconductor-to-insulator transition, Phys. Rev. B **48**, 4164 (1993).

[40] L. Merchant, J. Ostrick, R. P. Barber, Jr., and R. C. Dynes, Crossover from phase fluctuation to amplitude-dominated superconductivity: A model system, Phys. Rev. B **63**, 134508 (2001).

[41] S. L. Bud'ko, C. Petrovic, G. Lapertot, C. E. Cunningham, P. C. Canfield, M-H. Jung, and A. H. Lacerda, Magnetoresistivity and $H(T)$ in MgB_2, Phys. Rev. B **63**, 220503(R) (2001).

[42] C. U. Jung, M.-S. Park, W. N. Kang, M.-S. Kim, S. Y. Lee, and S.-I. Lee, Temperature- and magnetic-field-dependent resistivity of MgB_2 sintered at high-temperature and high-pressure condition, Physica C: Supercond. **353**, 162 (2001).

[43] I. Pallecchi, V. Braccini, E. G. d'Agliano, M. Monni, A. S. Siri, P. Manfrinetti, A. Palenzona, and M. Putti, Multiband magnetotransport in the normal state of MgB_2, Phys. Rev. B **71**, 104519 (2005).

[44] S. Bose, P. Raychaudhuri, R. Banerjee, and P. Ayyub, Upper critical field in nanostructured Nb: Competing effects of the reduction in density of states and the mean free path, Phys. Rev. B **74**, 224502 (2006).

[45] M. Tinkham, *Introduction to Superconductivity*, 2nd ed. (Dover, New York, 1996).

[46] A. K. Geim, I. V. Grigorieva, S. V. Dubonos, J. G. S. Lok, J. C. Maan, A. E. Filippov, and F. M. Peeters, Phase transitions in individual sub-micrometre superconductor, Nature (London) **390**, 259 (1997).

[47] B. J. Baelus and F. M. Peeters, Dependence of the vortex configuration on the geometry of mesoscopic flat samples, Phys. Rev. B **65**, 104515 (2002).

[48] D. Saint-James, G. Sarma, and E. J. Thomas, *Type-II Superconductivity* (Pergamon, New York, 1969).

[49] J. H. Brewer, *Muon Spin Rotation Spectroscopy: Principles and Applications in Solid State Physics* (Adam Hilger, Bristol, 1985).

[50] E. H. Brandt and A. Seeger, Muon-spin rotation as a tool for investigating the diffusion of positive muons in type-II superconductor, Adv. Phys. **35**, 189 (1986).

[51] J. E. Sonier, J. H. Brewer, and R. F. Kiefl, μSR studies of the vortex state in type-II superconductors, Rev. Mod. Phys. **72**, 769 (2000).

[52] R. E. Walstedt and L. R. Walker, Nuclear-resonance line shapes due to magnetic impurities in metals, Phys. Rev. B **9**, 4857 (1974).

[53] D. E. MacLaughlin, J. E. Sonier, R. H. Heffner, O. O. Bernal, Ben-Li Young, M. S. Rose, G. D. Morris, E. D. Bauer, T. D. Do, and M. B. Maple, Muon Spin Relaxation and Isotropic Pairing in Superconducting PrOs4Sb12, Phys. Rev. Lett. **89**, 157001 (2002).

[54] S. L. Lee, P. Zimmermann, H. Keller, M. Warden, I. M. Savić, R. Schauwecker, D. Zech, R. Cubitt, E. M. Forgan, P. H. Kes, T. W. Li, A. A. Menovsky, and Z. Tarnawski, Evidence for Flux-Lattice Melting and a Dimensional Crossover in Single-Crystal $Bi_{2.15}Sr_{1.85}CaCu_2O_{8+\delta}$ from Muon Spin Rotation Studies, Phys. Rev. Lett. **71**, 3862 (1993).

[55] J. E. Sonier, W. Huang, C. V. Kaiser, C. Cochrane, V. Pacradouni, S. A. Sabok-Sayr, M. D. Lumsden, B. C. Sales, M. A. McGuire, A. S. Sefat, and D. Mandrus, Magnetism and Disorder Effects on Muon Spin Rotation Measurements of the Magnetic Penetration Depth in Iron-Arsenic Superconductors, Phys. Rev. Lett. **106**, 127002 (2011).

[56] C. Niedermayer, C. Bernhard, T. Holden, R. K. Kremer, and K. Ahn, Muon spin relaxation study of the magnetic penetration depth in MgB_2, Phys. Rev. B **65**, 094512 (2002).

[57] K. Ohishi, T. Muranaka, J. Akimitsu, A. Koda, W. Higemoto, and R. Kadono, Quasiparticle excitations outside the vortex cores in MgB_2 probed by muon spin rotation, J. Phys. Soc. Jpn. **72**, 29 (2003).

[58] A. Shengelaya, C. M. Aegerter, S. Romer, H. Keller, P. W. Klamut, R. Dybzinski, B. Dabrowski, I. M. Savić, and J. Klamu, Muon-spin-rotation measurements of the penetration depth in the $YBa_2Cu_4O_8$ family of superconductors, Phys. Rev. B **58**, 3457 (1998).

[59] P. K. Biswas, A. Kreisel, Q. Wang, D. T. Adroja, A. D. Hillier, J. Zhao, R. Khasanov, J.-C. Orain, A. Amato, and E. Morenzoni, Evidence of nodal gap structure in the basal plane of the FeSe superconductor, Phys. Rev. B **98**, 180501(R) (2018).

[60] E. Roddick and D. Stroud, Effect of Phase Fluctuations on the Low-Temperature Penetration Depth of High-T_c superconductors, Phys. Rev. Lett. **74**, 1430 (1995).

[61] B. Sacépé, J. Seidemann, F. Gay, K. Davenport, A. Rogachev, M. Ovadia, K. Michaeli, and M. V. Feigel'man, Low-temperature anomaly in disordered superconductors near B_{c2} as a vortex-glass property, Nat. Phys. **15**, 48 (2019).

[62] J. E. Sonier, K. F. Poon, G. M. Luke, P. Kyriakou, R. I. Miller, R. Liang, C. R. Wiebe, P. Fournier, and R. L. Greene, Superconductivity and Field-Induced Magnetism in $Pr_{2-x}Ce_xCuO_4$ Single Crystals, Phys. Rev. Lett. **91**, 147002 (2003).

[63] R. Kadono, K. Ohishi, A. Koda, W. Higemoto, K. M. Kojima, M. Fujita, S. Kuroshima, and K. Yamada, Strong correlation between field-induced magnetism and superconductivity in $Pr_{0.89}LaCe_{0.11}CuO_4$, J. Phys. Soc. Jpn. **73**, 2944 (2004).

[64] R. Khasanov, A. Maisuradze, H. Maeter, A. Kwadrin, H. Luetkens, A. Amato, W. Schnelle, H. Rosner, A. Leithe-Jasper, and H.-H. Klauss, Superconductivity and Field-Induced Magnetism in $SrFe_{1.75}Co_{0.25}As_2$, Phys. Rev. Lett. **103**, 067010 (2009).

[65] T. J. Williams, A. A. Aczel, E. Baggio-Saitovitch, S. L. Bud'ko, P. C. Canfield, J. P. Carlo, T. Goko, H. Kageyama, A. Kitada, J. Munevar, N. Ni, S. R. Saha, K. Kirschenbaum, J. Paglione, D. R. Sanchez-Candela, Y. J. Uemura, and G. M. Luke, Superfluid density and field-induced magnetism in $Ba(Fe_{1-x}Co_x)_2As_2$ and $Sr(Fe_{1-x}Co_x)_2As_2$ measured with muon spin relaxation, Phys. Rev. B **82**, 094512 (2010).

[66] W. Braunisch, N. Knauf, V. Kataev, S. Neuhausen, A. Grutz, A. Kock, B. Roden, D. Khomskii, and D. Wohlleben, Paramagnetic Meissner Effect in Bi High-Temperature Superconductors, Phys. Rev. Lett. **68**, 1908 (1992).

[67] M. Sigrist and T. M. Rice, Unusual paramagnetic Meissner phenomena in granular high-temperature superconductors—A consequence of *d*-wave pairing? Rev. Mod. Phys. **67**, 503 (1995).

[68] E. H. Brandt, Precision Ginzburg-Landau Solution of Ideal Vortex Lattices for Any Induction and Symmetry, Phys. Rev. Lett. **78**, 2208 (1997).

[69] J. C. Cuevas and F. S. Bergeret, Magnetic Interference Patterns and Vortices in Diffusive SNS Junctions, Phys. Rev. Lett. **99**, 217002 (2007).

[70] D. Roditchev, C. Brun, L. Serrier-Garcia, J. C. Cuevas, V. Henrique L. Bessa, M. V. Milošević, F. Debontridder, V. Stolyarov, and T. Cren, Direct observation of Josephson vortex cores, Nat. Phys. **11**, 332 (2015).

[71] D. R. Harshman, E. H. Brandt, A. T. Fiory, M. Inui, D. B. Mitzi, L. F. Schneemeyer, and J. V. Waszczak, Longitudinal disordering of vortex lattices in anisotropic superconductors, Phys. Rev. B **47**, 2905 (1993).

[72] Y. M. Strelniker, A. Frydman, and S. Havlin, Percolation model for the superconductor-insulator transition in granular films, Phys. Rev. B **76**, 224528 (2007).

[73] N. Poccia, T. I. Baturina, F. Coneri, C. G. Molenaar, X. R. Wang, G. Bianconi, A. Brinkman, H. Hilgenkamp, A. A. Golubov, and V. M. Vinokur, Critical behavior at a dynamic vortex insulator-to-metal transition, Science **349**, 1202 (2015).

[74] M. Lankhorst, N. Poccia, M. P. Stehno, A. Galda, H. Barman, F. Coneri, H. Hilgenkamp, A. Brinkman, A. A. Golubov, V. Tripathi, T. I. Baturina, and V. M. Vinokur, Scaling universality at the dynamic vortex Mott transition, Phys. Rev. B **97**, 020504 (2018).

[75] S. M. Chudinov, R. Ferretti, S. Fusari, G. Mancini, and S. Stizza, Reentrant superconductivity mechanisms in amorphous carbon-silicon films containing tungsten, Phys. Rev. B **62**, 12516 (2000).

[76] J. Li, J. Pelliciari, C. Mazzoli, S. Catalano, F. Simmons, J. T. Sadowski, A. Levitan, M. Gibert, E. Carlson, J.-M. Triscone, S. Wilkins, and R. Comin, Scale-invariant magnetic textures in the strongly correlated oxide $NdNiO_3$, Nat. Commun. **10**, 4568 (2019).

[77] B. Pannetier and H. Courtois, Andreev reflection and proximity effect, J. Low Temp. Phys. **118**, 599 (2000).

[78] T. M. Klapwijk, Proximity effect from an Andreev perspective, J. Supercond. **17**, 593 (2004).

[79] B. J. van Wees, P. de Vries, P. Magnée, and T. M. Klapwijk, Excess Conductance of Superconductor-Semiconductor Interfaces Due to Phase Conjugation Between Electrons and Holes, Phys. Rev. Lett. **69**, 510 (1992).

[80] G. Deutscher, Andreev–Saint-James reflections: A probe of cuprate superconductors, Rev. Mod. Phys. **77**, 109 (2005).

[81] D. Garlaschelli, A. Capocci, and G. Caldarelli, Self-organized network evolution coupled to extremal dynamics, Nat. Phys. **3**, 813 (2007).

[82] J. Gómez-Gardeñes, S. Gómez, A. Arenas, and Y. Moreno, Explosive Synchronization Transitions in Scale-Free Networks, Phys. Rev. Lett. **106**, 128701 (2011).